RESEARCH ARTICLE

Key Points:
- Benthic oxygen fluxes vary by up to 25 times in North Sea permeable sediments
- Bottom boundary layer turbulence drives sediment O_2 flux in permeable sediments
- Bottom roughness coefficient varies as a function of velocity

Correspondence to:
D. F. McGinnis,
daniel.mcginnis@unige.ch

Quantifying tidally driven benthic oxygen exchange across permeable sediments: An aquatic eddy correlation study

Daniel F. McGinnis[1,2,3,4], Stefan Sommer[1], Andreas Lorke[5], Ronnie N. Glud[3,6,7], and Peter Linke[1]

[1]Helmholtz Centre for Ocean Research Kiel (GEOMAR), Kiel, Germany, [2]Department of Experimental Limnology, Leibniz-Institute of Freshwater Ecology and Inland Fisheries (IGB), Berlin, Germany, [3]Institute of Biology, Nordic Center for Earth Evolution, University of Southern Denmark, Odense M, Denmark, [4]Now at Earth and Environmental Sciences, Faculty of Sciences, University of Geneva, Geneva, Switzerland, [5]Institute for Environmental Sciences, University of Koblenz-Landau, Landau, Germany, [6]Scottish Association for Marine Science, Scottish Marine Institute, Oban, UK, [7]Arctic Research Centre, University of Aarhus, Aarhus C, Denmark

Abstract Continental shelves are predominately ($\sim$70%) covered with permeable, sandy sediments. While identified as critical sites for intense oxygen, carbon, and nutrient turnover, constituent exchange across permeable sediments remains poorly quantified. The central North Sea largely consists of permeable sediments and has been identified as increasingly at risk for developing hypoxia. Therefore, we investigate the benthic O_2 exchange across the permeable North Sea sediments using a combination of in situ micro-profiles, a benthic chamber, and aquatic eddy correlation. Tidal bottom currents drive the variable sediment O_2 penetration depth (from $\sim$3 to 8 mm) and the concurrent turbulence-driven 25-fold variation in the benthic sediment O_2 uptake. The O_2 flux and variability were reproduced using a simple 1-D model linking the benthic turbulence to the sediment pore water exchange. The high O_2 flux variability results from deeper sediment O_2 penetration depths and increased O_2 storage during high velocities, which is then utilized during low-flow periods. The study reveals that the benthic hydrodynamics, sediment permeability, and pore water redox oscillations are all intimately linked and crucial parameters determining the oxygen availability. These parameters must all be considered when evaluating mineralization pathways of organic matter and nutrients in permeable sediments.

1. Introduction

Continental shelf seas are dominated by sandy, permeable sediments [*Cook et al.*, 2007; *Emery*, 1968]. Research during the last decade has increasingly indicated that permeable sediments are regions of high organic carbon and nutrient turnover [*Precht and Huettel*, 2003]. The apparently high sediment reactivity is suggested to be facilitated by pore water advection [*Gihring et al.*, 2010; *Lohse et al.*, 1996; *Rusch et al.*, 2001] driven by flow interaction with bottom topography, density gradients, and wave motions [*Huettel et al.*, 2014; *Rocha*, 2008; *Santos et al.*, 2012]. Despite the importance of permeable sediment, in situ measurements of fluxes and pore water properties remain both challenging and limited [*Boudreau*, 2000; *Glud*, 2008].

Dissolved O_2 is utilized during aerobic respiration and for the oxidation of constituents from anaerobic respiration (e.g., H_2S, CH_4, NH_3, etc.) and is an important proxy for estimating total carbon turnover in aquatic systems [*Glud*, 2008]. Resolving O_2 fluxes across permeable sediments remains a true challenge, especially in situ, and reliable measurements of O_2 flux magnitude and variability are few [*Cook et al.*, 2007; *Janssen et al.*, 2005; *Reimers et al.*, 2004]. Traditional flux measurement techniques (i.e., chambers and microprofiles) are inadequate in permeable sediments as chambers exclude the natural hydrodynamics, microprofiles do not quantify pore water advection, and both provide only limited temporal resolution [*Glud et al.*, 2005; *Lohse et al.*, 1996; *Rocha*, 2008]. However, several flume [*Forster et al.*, 1996; *Reimers et al.*, 2004] and in situ [*Berg et al.*, 2013; *Cook et al.*, 2007; *de Beer et al.*, 2005; *Werner et al.*, 2006] studies have demonstrated that the hydrodynamics is a crucial driver of benthic O_2 dynamics in permeable sediments.

Originally used to resolve net ecosystem exchange in terrestrial environments [*Baldocchi*, 2003], the noninvasive eddy correlation (EC) technique overcomes these limitations by integrating the flux over a "footprint" area of many m^2 and therefore adequately captures both the bioturbation and natural hydrodynamics [*Berg et al.*, 2007]. The resolved hydrodynamic data allow for detailed analyses of the turbulence relationship
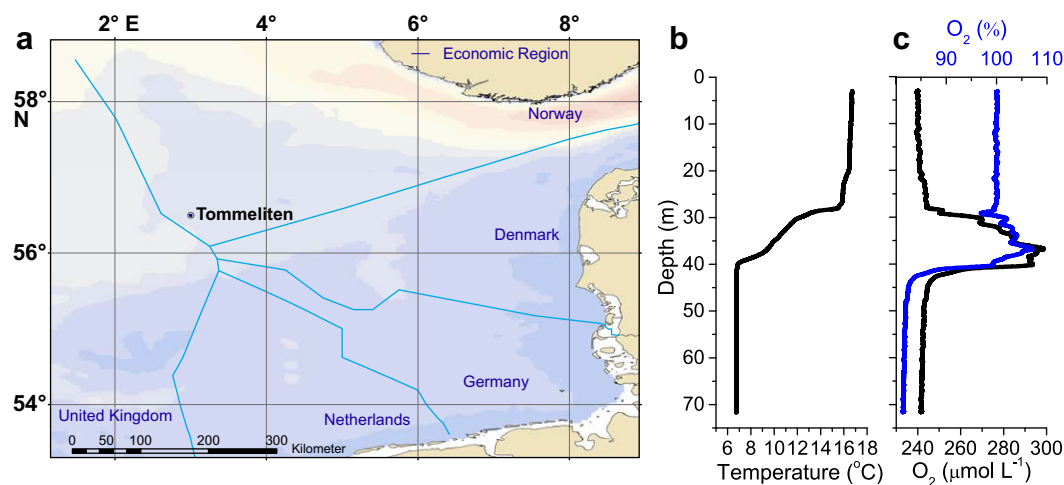
Figure 1. (a) Tommeliten study site (56.5°N, 3.0°E; ∼74 m deep) in the Norwegian sector of the North Sea. (right) CTD profile nearby the study site showing (b) temperature and (c) O_2 profiles at the North Sea study site.

to the benthic O_2 uptake [*Lorke et al.*, 2012]. The EC technique has been applied for measuring O_2 fluxes in various complex aquatic environments where traditional methods often fail [*Holtappels et al.*, 2013, and references therein]. Several recent studies have now demonstrated the applicability of the EC technique in permeable sediments [*Berg et al.*, 2013; *McCann-Grosvenor et al.*, 2014; *Reimers et al.*, 2012].

Although sandy, permeable sediments cover ∼70% of the North Sea, most benthic flux research has focused either on muddy areas [*de Beer et al.*, 2005] or permeable sediments at shallow, nearshore environments [*Huettel et al.*, 2014, and references therein]. While there has been a trend of decreasing oxygen levels in the central North Sea [*Greenwood et al.*, 2010, and references therein], the role of the sediment processes remains unclear [*Weston et al.*, 2008]. Therefore, we investigate the benthic boundary layer (BBL) turbulence and O_2 turnover in the permeable sediments of the central North Sea using a suite of state-of-the-art benthic flux measurement techniques.

The specific objectives of our study are to:

1. Resolve the BBL turbulence and sediment-water O_2 exchange in central North Sea permeable sediments using two benthic eddy correlation landers, a sediment microprofiler lander, and a benthic flux chamber.
2. To investigate the flux drivers using a 1-D modeling study linking the BBL turbulence to the permeable-sediment pore water exchange.
3. Use the combined results and gained insights to discuss the importance of tidally driven turbulence for in situ benthic exchange rates in coastal, permeable sediments.

2. Study Site, Instrumentation, and Methods

2.1. General Setting

The study was carried out during RV Celtic Explorer cruise CE0913 (26 July to 14 August 2009) at Tommeliten, located on the European shelf in the central North Sea (Figure 1a). The study site is characterized by strong pelagic stratification during summer, a relatively shallow depth (∼74 m), and a 35 m bottom mixed layer (Figure 1b) [*Schneider von Deimling et al.*, 2011]. While Tommeliten is a well-known methane seepage area [see *Schneider von Deimling et al.*, 2011, and references therein], we deployed well away from these sites and in an area absent of any seep-related fauna, and any obvious methane seepage (i.e., bubbles). Measured water column methane concentrations were very low (<100 nM). As assessed by photo and video surveys, our study area appeared to be homogeneous—sandy with small ripples and a marked absence of benthic fauna or large roughness elements (i.e., rocks, shells, etc.). From photographs, the ripples were estimated to be about 0.5 cm high (valley to peak) and about 2–3 cm long (peak to peak).

Table 1. Instrument Coordinates and Deployment Times

Coordinates		Instrument	Deployment	Retrieval
56.502117	3.002212	Profiler Lander	9 Aug 11:40	10 Aug 14:00
56.502133	3.002233	EC1 (Sophia)	9 Aug 14:09	11 Aug 09:01
56.502133[a]	3.002233	Benthic Chamber	9 Aug 14:17	10 Aug 19:38
56.501400	3.001367	EC2 (Galina)	9 Aug 18:58	11 Aug 10:15
56.498683	2.995245	CTD 18	8 Aug 11:25	
56.498593	2.996320	CTD 19	8 Aug 19:30	

[a]About 10 m from EC1.

2.2. Instrumentation

The instruments, described below, were deployed over ∼3 tidal cycles (Table 1) within about 100 m of each other.

2.2.1. Eddy Correlation Landers

The eddy correlation (EC) instrument is an autonomous benthic lander designed to measure turbulent oxygen fluxes (Figure 2, left). The EC consists of a deep-water Acoustic Doppler Velocimeter (ADV; Vector, Nortek, Norway), an integrated oxygen picoamplifier [*McGinnis et al.*, 2011] with microelectrode, and deployment frame. The oxygen microelectrode is a Clark type with a fast response time ($t_{90} < 0.3$ s) and a 10 μm tip diameter [*Gundersen et al.*, 1998; *Revsbech*, 1989]. The tip of the microelectrode was positioned as close as possible but without entering the ADV sampling volume, which is located 0.15 m below the transducer. ADV velocity and O_2 data are logged at 64 Hz.

The O_2 microelectrodes were calibrated onboard at bottom water temperature using a 0 and 100% O_2 solution prepared with ambient water, and O_2 sensor readings were compared to water column CTD O_2 profiles (the EC system logged on the way down and up), and with bottom optode O_2 readings obtained from the nearby Profiler Lander. Two EC devices (EC1 and EC2) were deployed within several hours of each other using the ROV KIEL6000 (http://www.geomar.de/en/centre/central-facilities/tlz/rovkiel6000/overview/) and separated by ∼100 m (Table 1). EC1 and EC2 were deployed with their sampling volume 8 and 12 cm above the bottom, respectively, and facing the approximate stream-wise current direction but in opposite directions. In principle, assuming a homogeneous sediment oxygen sink, the differences in deployment heights would not affect the fluxes (the flux should be constant with depth in the BBL).
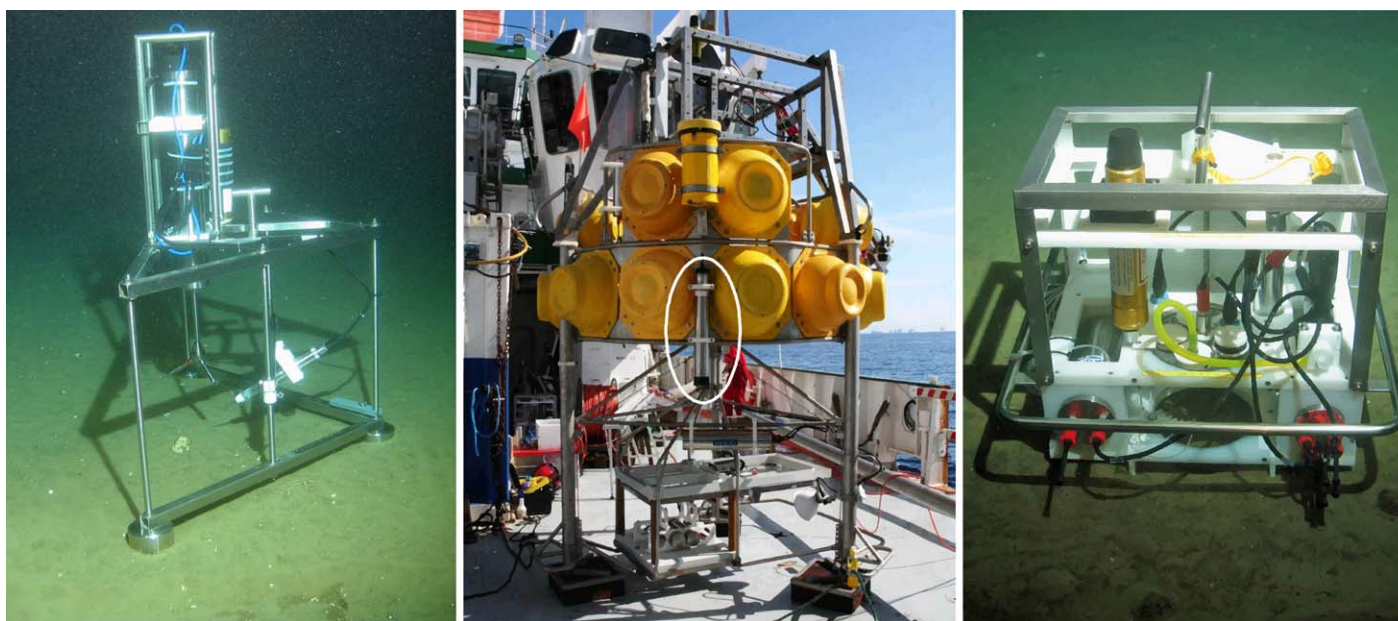

Figure 2. (left) The deployed eddy correlation lander 1 (EC1). (middle) Transecting profiler lander together with downward facing Acoustic Doppler Profiler (white circle; ADP). (right) Benthic chamber.

2.2.2. Transecting Profiler Lander

Oxygen microprofiles were obtained by the nearby transecting profile lander over ∼24 h period corresponding with the EC deployment (Figure 2, middle). The lander belongs to the series of the GEOMAR Lander System (GML), which is based on a tripod-shaped universal platform capable of supporting different scientific payloads [*Pfannkuche and Linke*, 2003]. The lander is deployed by a launcher with online video transmission allowing a soft and targeted deployment on the seafloor. The major component is a profiler which moves the microelectrodes in the *x*, *y*, and *z* directions at the seafloor to resolve high-resolution oxygen profiles in the sediment. A digital camera system (Ocean Imaging Systems) is attached to the legs of the lander to provide close up images of the sensors and the sediment surface.

2.2.3. Benthic Chamber

The Benthic Chamber (BC; Figure 2, right) is designed to measure benthic fluxes of dissolved chemical species over time at the sediment-water interface. It contains a cylindrical chamber (20 cm diameter), which is pushed into the sediment by the ROV, and a small stirrer which rotates at 144 rpm and mixes the contained water. Using the mixing speed and stirrer geometry, we estimated the turbulence to be ∼2–3 $\times 10^{-7}$ W kg^{-1}. The displaced water in the chamber is pushed through a nonreturn valve, and any resuspended matter is removed by flushing the overlying water with a small submersible pump (SBE5). The BC carries two oxygen optodes (Aanderaa, Norway), one inside and one outside of the chamber. The chamber is self-contained with its own power supply. A transponder (Sonardyne, UK) is added for recovery by the ROV.

2.2.4. Acoustic Doppler Profiler

The Aquadopp Acoustic Doppler current profiler (ADP, Nortek, Norway) was downward facing and mounted to the transecting profiler frame (Figure 2, middle, white circle). The ADP (2 MHz) was in high-resolution mode and collected burst data in *xyz* coordinates; 2048 samples at 8 Hz every 900 s. The total profiling range was to the bottom (1.6 m) with bin sizes of 30 mm.

2.2.5. Conductivity-Temperature-Depth (CTD) Profiler

The SBE9 Seabird CTD was the shipboard CTD and sampled at 24 Hz. The CTD was equipped with temperature, conductivity, pressure, oxygen, light transmission, and pH. A 24 carousel Rosette system was installed for discrete water sampling.

2.3. ADV and Eddy Correlation Data Treatment
2.3.1. ADV Preprocessing

The following protocol is used to improve the ADV velocity data quality. These protocols are also summarized at http://sohfea.dfmcginnis.com/ in the user manual and also described elsewhere [e.g., *Glud et al.*, 2014; *Lorrai et al.*, 2010]. The pre- and postprocessing executable programs are also available at the website.

1. Bin average: the time series are bin-averaged from 64 to 32 Hz. In the process, low-quality data points are removed and excluded from the average. To ensure high-quality turbulence data, velocity data points are excluded when the beam correlation falls below 70%.
2. Despike: next, the averaged velocity data are despiked using an acceleration threshold method [*Goring and Nikora*, 2002]. The local acceleration is calculated between neighboring data points as $A_i = \Delta V_i/\Delta t$, where i denotes the *x*, *y*, and *z* components of velocity. A velocity data point is discarded if the absolute value of $A_i > \alpha$, where α varies between 1 and 1.5 in the horizontal, and between 0.3 and 1 in the vertical. The α criteria are selected based on experience [*Goring and Nikora*, 2002] and are therefore subjective. Discarded velocity date points are replaced by interpolating between the neighboring data points. In our case, $\alpha = 0.3$ for the vertical despiking provided reasonable results and resulted in <0.001% of the data being discarded. The data are carefully evaluated afterward to ensure that real fluctuations are not excluded.
3. Rotation: data are rotated using the planar fit method [*Wilczak et al.*, 2001]. This method, compared with simpler rotations (double or triple rotation), was found to best remove the horizontal projection of fluxes into the vertical velocity component, which could strongly alter fluxes [*Lorke et al.*, 2013, 2012]. The rotation aligns the vertical velocity vector normal to the horizontal streamline velocity. In this case, the three

rotations ultimately did not vary significantly. In the same step, the horizontal velocity data are rotated into their streamwise and transverse components before turbulence analyses are performed.

2.3.2. Turbulence Analyses

The power spectra were performed on the velocity data using the Matlab power spectral density (PSD) function with a Hanning window and linear detrending (NFFT = 8192, overlap = 4096). Power spectra and dissipation (ε) rates of total kinetic energy (TKE) are evaluated for possible flow interference from upstream obstructions. Frame or object interference is inferred by altered ε-velocity relations, which are also revealed in the spectral structure. Turbulence analyses are also used to select the appropriate eddy window—the window that covers all the eddy contributions but excludes low-frequency nonturbulent contributions [*McGinnis et al.*, 2008]. The dissipation of TKE was solved using the inertial dissipation method (IDM) [*Bluteau et al.*, 2011], and shear velocities u_* were additionally solved using LOW formulations [see *Inoue et al.*, 2011, equation (2)].

2.3.3. Law-Of-The-Wall

Confirming the assumptions underlying LOW scaling is important for depth-extrapolation of turbulent diffusivities $K_z(z)$ in the BBL and other important hydrodynamic properties. LOW-scaling, and the eddy correlation assumptions, also imply that the O_2 flux is constant with depth in the turbulent BBL. Measured BBL velocity profiles are used to confirm LOW assumptions, where the velocity u can be described as a function of distance from the bottom (z) as

$$u(z) = \frac{u_*}{\kappa} \ln\left(\frac{z}{z_o}\right) = (\varepsilon_z z)^{1/3} \kappa^{-2/3} \ln\left(\frac{z}{z_o}\right), \qquad (1)$$

where z_o is roughness length, u_* the shear velocity, and κ is the von Kármán constant (0.4) [*Kundu and Cohen*, 2008]. The water column diffusivity is expressed as $K_z(z) = \kappa u_* z$.

2.3.4. Eddy Flux Extraction

Data are processed using the SOHFEA software (program and user guide available at http://sohfea.dfmcginnis.com/). The velocity and concentrations are broken down to their mean and fluctuating components $w(t) = \overline{w} + w'$ and $c(t) = \overline{c} + c'$, and the fluctuating components are extracted from the data by one of three detrending methods [*Moncrieff et al.*, 2004]. With the following assumptions, the time-averaged correlation of the turbulent O_2 fluctuations C' and vertical velocity fluctuations w' measured at some distance close (generally 5–15 cm) to the sediment represent the flux to the sediment $F = \overline{w'c'}$ [*Berg et al.*, 2003]. The primary assumptions are negligible horizontal flux divergence, negligible storage terms [*Holtappels et al.*, 2013], and a homogeneous oxygen uptake at the sediment-water interface. The fluxes were solved with linear detrending with a bin size between 10 and 60 s, depending on the frequency range of the flux contributing eddies (see section 3.2) [*Lorrai et al.*, 2010; *McGinnis et al.*, 2008].

To account for the time lag resulting from both the physical separation between the ADV measurement volume and sensor tip, the O_2 data are shifted in time relative to the velocity data to a maximum of 2 s to achieve the maximum correlation (i.e., the maximum negative flux) between the time series [*McGinnis et al.*, 2008]. The fluxes, dissipation rates of turbulent kinetic energy (TKE), and velocities were averaged with a 15 min running mean, and reported in 15 min intervals. This interval was a good balance between capturing the temporal dynamics while removing excess noise and intermittency.

2.4. Bottom-Boundary Layer/Sediment-Pore Water Model

The nonsteady state box model is developed similar to that by *Schmale et al.* [2011] and *Scalo et al.* [2013] and is essentially a 1-D discretized representation of Fick's second law, where

$$\frac{\partial C}{\partial t} = K_z \frac{\partial^2 c}{\partial z^2} + R_z. \qquad (2)$$

Table 2. Finite Difference Equations for the Box Model

Surface layer	$\frac{\Delta c_i}{\Delta t} = \frac{K_{Boundary}\left(c_{Boundary} - c_i\right)}{\Delta z_i^2} - \frac{K_{i,water}\left(c_i - c_{i+1}\right)}{\Delta z_i^2}$
Water side	$\frac{\Delta c_i}{\Delta t} = \frac{K_{i-1,water}\left(c_{i-1} - c_i\right)}{\Delta z_i^2} - \frac{K_{i,water}\left(c_i - c_{i+1}\right)}{\Delta z_i^2}$
Sediment-water interface	$\frac{\Delta c_i}{\Delta t} = \frac{K_{i-1,water}\left(c_{i-1} - c_i\right)}{\Delta z_i^2} - \frac{K_{i,sed}\left(c_i - c_{i+1}\right)}{\Delta z_i^2} + R_i$
Sediment side	$\frac{\Delta c_i}{\Delta t} = \frac{K_{i-1,sed}\left(c_{i-1} - c_i\right)}{\Delta z_i^2} - \frac{K_{i,sed}\left(c_i - c_{i+1}\right)}{\Delta z_i^2} + R_i$

The diffusion K is either the BBL turbulent or the effective bulk pore water diffusivity (m^2 s^{-1}), R (mmol m^{-3} s^{-1}) is the concentration reaction rate (c in mmol m^{-3}), and t is time. R on the water side is very low compared to the sediment R implying that the dissolved O_2 on the water side can be treated as a
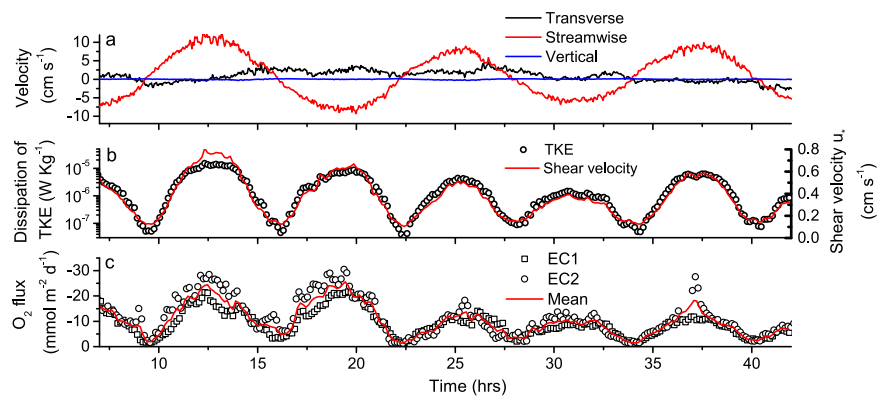
Figure 3. Measured and derived EC values. (a) Water velocity components from EC2 at 12 cm above the sediment-water interface, (b) left axis: 15 min running-mean dissipation rate of TKE (ε) from inertial dissipation method and, right axis: shear velocity (u_*). (c) Extracted eddy fluxes from both instruments and their combined average.

passive scalar (i.e., no water side O_2 consumption) [*Scalo et al.*, 2012]. The box model simulates vertical turbulent transport in the 1 m of the water column extending up from the sediment-water interface, which is linked to 2 cm depth of sediment below. The basic discretized equations for each box are shown in Table 2.

$c_{Boundary} = 230\ \mu$mol L^{-1} is the input oxygen concentration, which is constant at 1 m above the sediment-water interface, and Δz is the box thickness (set to 1 mm for the water side and 0.1 mm for the sediment side). The shear velocity u_* (Figure 3b) is used to solve for the turbulent diffusivity as a function of depth and time using the LOW; $K(z) = \kappa u_* z$ and $K_{Boundary1m} = \kappa u_* (1\ m)$. The diffusive boundary layer thickness at the sediment-water interface is calculated according to *Lorke and Peeters* [2006].

3. Results Part I: Turbulence and Hydrodynamics

The basic and derived properties over the deployment are shown in Figure 3. The hydrodynamic forcing is dominated by the lunar semidiurnal (M_2) tide with $\sim$12 h period (Figure 3a). The sediment generally consists of fine, well-sorted rippled sand and occasional shells. The sediment has a laboratory measured permeability of $k = 6.6 \times 10^{-12}$ m^2 (over the surface 2 cm of sediment). Permeable sediments are defined as those with a permeability $k > 10^{-12}$ m^2 [*Huettel et al.*, 2014].

The average sediment, water column, and range of hydrodynamic properties are summarized in Table 3. Figure 3a shows the typical current velocities over the deployment, the range of ε and shear velocity u_*, and the extracted fluxes (and mean) from both instruments. The following sections describe the turbulence evaluation procedure, eddy contribution range, and the extraction of the benthic oxygen fluxes in greater detail.

3.1. Flow Interference
Dissipation rates (ε) solved using IDM are plotted as a function of velocity (Figure 4a) and are used to reveal outliers due to frame interference or other obstructions. Using the trendline shown in Figure 4a, the

Table 3. Measured Sediment, Water Column, and Hydrodynamic Properties

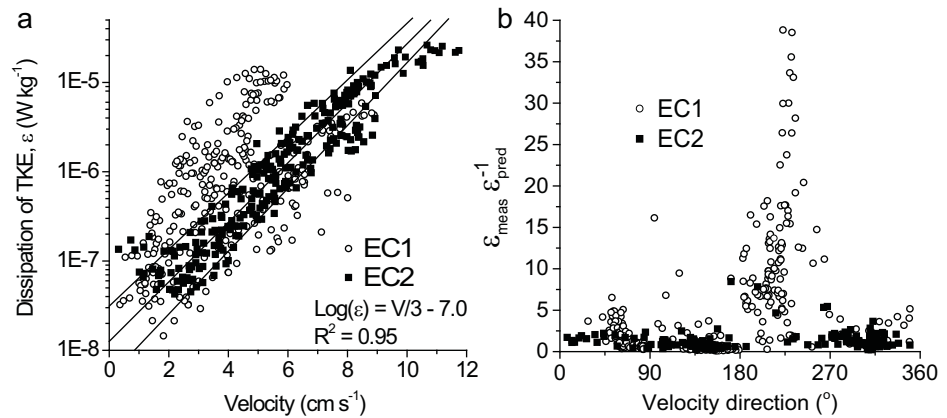| Parameter	Symbol	Unit	Mean	STD
Sediment permeability	k	m^2	6.6×10^{-12}	1.2×10^{-13}
Sediment porosity	δ		0.43	
O_2 (BBL)	O_2	μmol L^{-1}	230 (75% sat)	1
Temperature (BBL)	T	°C	6.8	0.1
Salinity (BBL)	S	psu	35.1	
			Min	Max
Velocity at 12 cm height	u	cm s^{-1}	0.3	11.7
Dissipation rate (at 12 cm) TKE	ε	W kg^{-1}	3×10^{-8}	1.5×10^{-5}
Shear velocity	u_*	cm s^{-1}	0.1	0.8

Figure 4. (a) Relationship between ε and water velocity. Data falling outside of the 95% error bands are flagged. (b) Deviation of measured versus predicted ε from relationship in Figure 4a. Most significant deviations occur in EC1 data when flow is from 180 to 270°, which is over the crossbar.

measured dissipations are then divided by the predicted dissipations (Figure 4b). Elevated dissipation rates become obvious (up to a factor 40) when the flow is coming over the frame of EC1 (direction 180–270°). EC1 is more susceptible to this cross-bar frame interference, as it is deployed more closely to the bottom (8 versus 12 cm for EC2).

3.2. Turbulent Eddy Time and Length Scales

The vertical distribution of the current velocity, shear velocity, and dissipation of TKE in the BBL can be described by one-dimensional boundary layer theory, i.e., LOW. Figure 5a shows the 15 min averaged profiles, read from right to left in the time sequence, showing good agreement to the LOW theoretic velocity profile (equation (1)). Additionally, good agreement between ε from the IDM with the LOW formulation for the shear velocity u_* provides further confirmation of LOW assumptions, as the IDM is independent of the LOW assumptions and $\varepsilon(z) = u_*^3/\kappa z$ ($R^2 = 0.94$).

Using LOW formulations, we calculate basic hydrodynamic properties and expected eddy sizes and length scales (Table 4) similar to the analyses performed by *Lorrai et al.* [2010]. The example analyses in Table 4 and Figure 5b are based on two hours of data during low (hour 9.0) and high (hour 12.0) velocities. The largest eddies are a function of the deployment distance of the EC sampling volume to the sediment surface. The timescale of the largest eddy (slowest timescales) is a crucial cutoff for the eddy analyses, as using
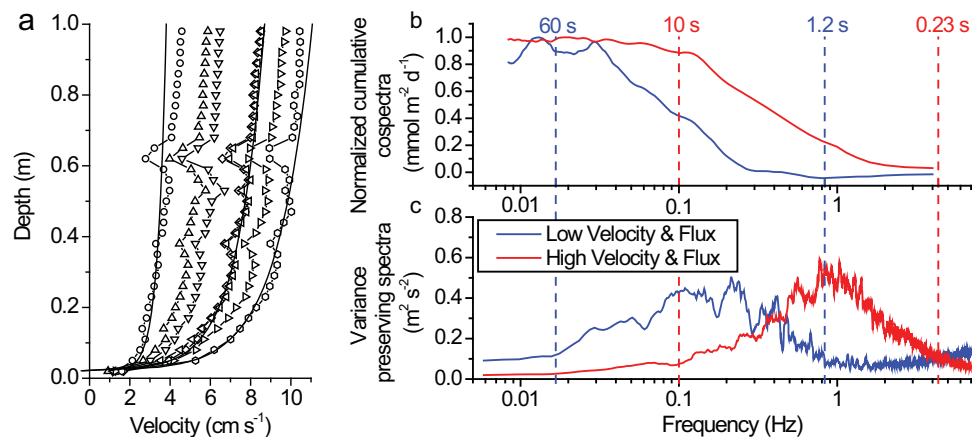

Figure 5. (a) Boundary layer velocity profiles obtained from the high-resolution, downward-facing Acoustic Doppler Profiler (ADP) showing the current slowing down over ∼2 h, and the fit to the theoretical Law-of-the-Wall (LOW) profiles shown as solid lines. (b) Normalized cumulative cospectra [see *McGinnis et al.*, 2008]. (c) Normalized variance preserving spectra performed on the vertical velocity. Both plots illustrate eddy spectral contribution ranges.

Table 4. Summary of Turbulence and Scaling Parameters[a]

Description			Formulation	Low	High
Hour analyzed		h		9.0	12.0
Velocity magnitude	u	m s^{-1}		0.024	0.109
Kinematic viscosity	ν	m^2 s^{-1}	at 6°C	1.4×10^{-6}	1.4×10^{-6}
Dissipation of TKE	ε	W kg^{-1}	ID method	9×10^{-8}	2×10^{-5}
Shear velocity	u_*	m s^{-1}	$u_* = (\varepsilon \kappa z)^{1/3}$	0.0012	0.010
Bottom drag	C_{1m}		$C_{1m} = (u_*/u_{1m})^2$	0.005	0.0088
Roughness length	z_o	m	$z_o = z \times \exp(-u_z \kappa / u_*)$	$1.4 \times 10^{-4\ c}$	0.0053
Smallest eddy size	L	m	$L = 2\pi (\nu^3/\varepsilon)^{1/4}$	0.015	0.004
Observed[b] (calculated) timescale largest eddies V_z	τ_{OBS}	s	$\tau = z/u_*$	60 (103)	10 (12)
Observed[b] (calculated) timescale smallest eddies V_z	τ_{OBS}	s	$\tau = (L^2/\varepsilon)^{1/3}$	1.2 (4)	0.23 (0.3)

[a]Time and length scales estimated from Figure 5b are compared with theoretical LOW scaling [see *Lorrai et al.*, 2010, Table 1].
[b]Obtained from Figure 5.
[c]Smooth flow regime $z_o \approx 0.1\ \nu/u$.

longer timescales may introduce signals from low-frequency basin-scale waves, convective mixing, or other nonturbulent interfering contributions [*McGinnis et al.*, 2008].

According to Figures 5b and 5c, the spectral contributions range spans ∼2 orders of magnitude, from 1.2 s to about 60 s for the low velocity case, and shifted about 1 order of magnitude toward higher frequency for the high velocity case (0.23–10 s). These observed values of the cutoff frequencies agree well with calculated values (Table 3). The eddy flux window size was set using a window that is slightly (∼25%) larger than the largest calculated turbulent eddy at a given velocity.

3.3. Variable Bottom Drag and Roughness

The hydraulic roughness drives the BBL turbulence and is expressed as either the bottom drag coefficient, C_{1m}, or the bottom roughness length, z_o. Both parameters represent the frictional force exerted on the BBL water flow by the sediment surface [*Lefebvre et al.*, 2011] and are related by *Lorke et al.* [2002]

$$C_{1m} = \left(\frac{\kappa}{\ln(z_0^{-1})} \right)^2. \tag{3}$$

The hydraulic roughness is treated as a constant within aquatic systems; however, our C_{1m} values are variable and increase with velocity magnitudes (measured at 12 cm above the bottom) both below and above ∼3.5 cm s^{-1} (Figure 6a). The highest average C_{1m} value is 0.0042 at 1.5 cm s^{-1} (we measured 0.0063 at 1 cm s^{-1}), which then falls to a minimum of 0.0018 at 3.5 cm s^{-1}, then doubles again to 0.0036 at our
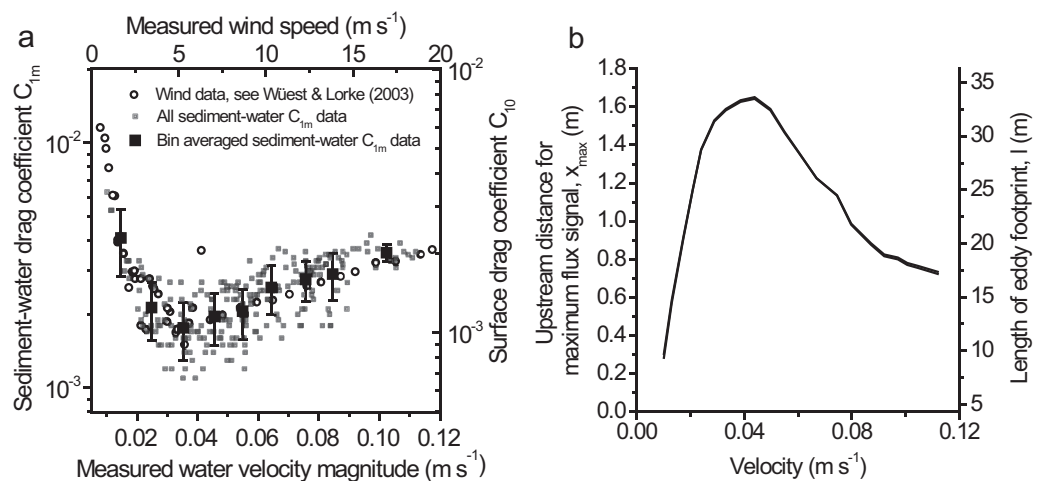

Figure 6. (a) Bottom drag coefficient related to the surface drag coefficient from wind data. Data scaled to wind drag coefficient data compiled by *Wüest and Lorke* [2003]. Velocity magnitude measured at 12 cm above the seafloor (EC2). (b) Calculated footprint length from *Berg et al.* [2007] as a function of water velocity in our system: x_{max} is the upstream distance of the maximum flux signal, and l is the length of the footprint.
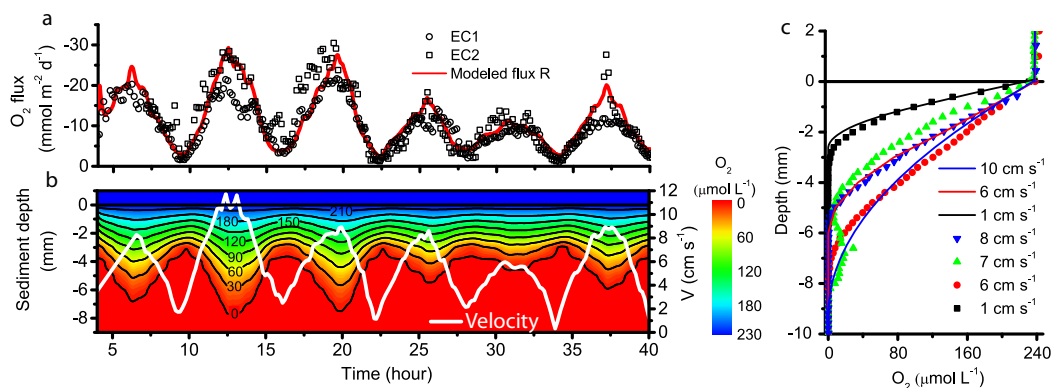
Figure 7. (a) Modeling results using measured EC2 shear velocity u_* as model input. Figure shows predicted eddy fluxes for sediment O_2 consumption rates, R = 0.05 mmol m^{-3} s^{-1} (red curve) compared to measured fluxes (open symbols). (b) Predicted sediment pore water O_2 concentration contour with EC2 (12 cm above bottom) measured water velocity magnitude overlaid. (c) Examples of measured and modeled O_2 pore water profiles (line) over the velocity range, and measured values (symbols). Measured profiles were vertically aligned to the estimated position of the sediment surface.

maximum velocity of 10.2 cm s^{-1}. As they are relatable with equation (3), the same trend is also observed for z_o. Interestingly, our measured C_{1m} values scale well with those for wind drag data compiled in *Wüest and Lorke* [2003], implying that surface wave roughness acts similarly to ripples (Figure 6a).

Due to the presence of small ripples, the total friction acting on the BBL flow becomes a combination of the roughness imparted by the grain size and the roughness resulting from the ripples [*Lefebvre et al.*, 2011]. The minimum friction (drag) coefficient C_{1m} occurred at ~3.5 cm s^{-1} (Figure 6a). We speculate that the increasing C_{1m} at velocity magnitudes greater than ~3.5 cm s^{-1} (measured at 12 cm) is the transition where the small ripples begin to dominate the roughness instead of the grain size. *Lefebvre et al.* [2011] also found a dependence on z_o with velocity, as well as tidal direction, though their velocity range and bed form sizes were much larger than those reported here. *Cheng et al.* [1999] reported drag coefficients were in the range of 0.002–0.006 similar to ours, with their high values for bottom roughness also correlating with their lowest velocities. The presence of ripples therefore effects the turbulence, pore water exchange, and the resulting variable bottom roughness will result in a flow-dependent eddy flux footprint (Figure 6b; discussed below) [*Berg et al.*, 2007].

4. Results Part II: Benthic Oxygen Flux

The observed EC fluxes varied by a factor of up to 25, from −1.2 up to −30.5 mmol m^{-2} d^{-1} (average −10.3 ± 6.3 mmol m^{-2} d^{-1}) over the tidal cycles (Figures 3c and 7a). EC fluxes were similar between both EC instruments (EC1 = −9.2 and EC2 = −11.3 mmol m^{-2} d^{-1}). The deployed benthic flux chamber resolved O_2 fluxes during this period of −7.0 mmol m^{-2} d^{-1}. The average O_2 penetration depth (OPD) measured with the profiling lander was 4.4 ± 1.2 mm and generally increased with flow velocity; ranging from ~3 mm at low velocity up to 7–8 mm at higher velocity (see example profiles, Figure 7c). However, fluxes from the profiles obtained from permeable sediment cannot be resolved without detailed quantitative knowledge of the advective pore water transport [*Berg et al.*, 1998; *de Beer et al.*, 2005]. Consequently, we developed a model approach to investigate the pore water dynamics within these sediments and the subsequent O_2 flux variability.

4.1. Benthic-Pore Water O_2 Model Results

The O_2 fluxes and dynamics were modeled using a simple, one-dimensional approach linking the BBL hydrodynamics to the sediment O_2 dynamics. Generally, the localized pore water advection acts on a centimeter-scale defined by the individual roughness elements (i.e., ripples) and flows as low as 3 cm s^{-1} over roughness elements down to 700 μm can already begin to induce advective pore water exchange in permeable sediments [*Huettel et al.*, 2014]. When integrating this small-scale (cm's) advection over a 10's m^2 footprint (i.e., the EC footprint [see *Berg et al.*, 2007]), then the net effect can be represented in the model as enhanced pore water diffusivity (dispersion), a common approach in 1-D permeable sediment models [see
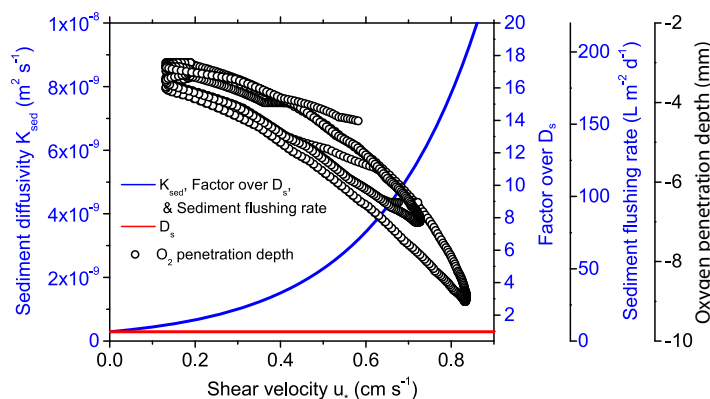
Figure 8. Modeled sediment diffusivity as a function of shear velocity (equation (4)), and the corresponding factor over molecular diffusion (first right axis). The second right axis gives the corresponding sediment flushing rate. The far right axis indicates the modeled oxygen penetration depth during the respective tidal cycles (open symbols on plot).

Boudreau, 2000, and references therein]. The model predicts the evolution of the sediment and BBL O_2 profiles and the turbulent O_2 fluxes in the water column (Figures 7a–7c) in response to the measured hydrodynamic forcing.

The temporally resolved shear velocity (u_*; Figure 3b) is used to define the vertical diffusivity $K_z(z) = \kappa u_* z$ throughout the BBL down to the sediment-water interface. The only degrees of freedom in the model are (1) the p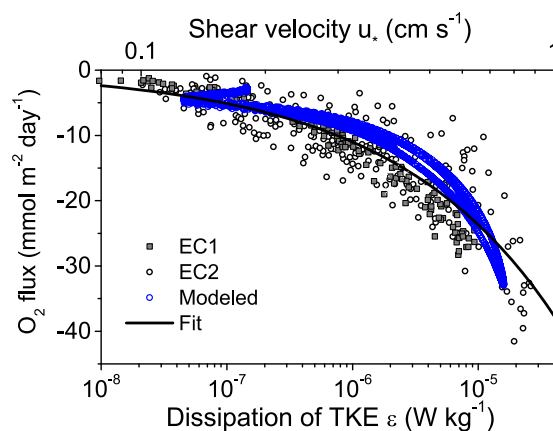ore water diffusivity and (2) the sediment O_2 consumption rate, R. We applied a temporally and spatially constant R = 0.05 mmol m^{-3} s^{-1} from permeable sediments in the Wadden Sea (North Sea) [*Polerecky et al.*, 2005]. The apparent bulk sediment diffusivity (i.e., pore water dispersion) K_{sed} is then estimated as a function of shear velocity u_* that best reproduces the measured O_2 eddy fluxes as

$$K_{sed} = D_s e^{\alpha \kappa u_*} \quad (m^2 s^{-1}), \tag{4}$$

where u_* in equation (4) is expressed in mm s^{-1}, and α is the fit parameter that should vary with sediment permeability. Coincidentally, in our case the best fit was achieved for $\alpha \approx 1$ s m^{-1}. D_s in equation (4) is the molecular diffusivity of O_2 in the sediment ($D_s = 2.93 \times 10^{-10}$ m^{2}s^{-1}), defined as $D_s = \theta DO_2$, where θ is the sediment tortuosity, a function of sediment type and porosity φ [*Ullman and Aller*, 1982]. Using the above listed boundary conditions, Figures 7a–7c show the predicted benthic O_2 flux and sediment O_2 concentration and penetration depth over time.

The predicted eddy fluxes in Figure 7a match the measured data from both deployed EC instruments ($r^2 > 0.94$) and captures the range of the flux variability. The model also reproduces the general shape of the measured O_2 microprofile curves and the range of oxygen penetration depths observed with the microprofiling lander (Figure 7c). The modeled sediment oxygen contour (Figure 7b) illustrates the bulk-average temporal evolution of the pore water O_2 concentration over the tidal cycles, and Figure 8 depicts the O_2 penetration versus u_*. According to the model, the oxygen penetration peak lags the velocity peak by about 0.3 h, which causes the hysteresis seen in the oxygen penetration depths (Figure 8).

5. Discussion

5.1. Sediment Flushing

In natural sediments, the enhanced diffusion, or small-scale advection, is driven by, e.g., flow interaction with bottom topography, density and pressure gradients, migrating ripples, and wave motions [*Huettel and Webster*, 2001; *Huettel et al.*, 2014, and references therein]. A convenient way to conceptualize the enhanced bulk diffusivity (i.e., pore water advection) is as sediment flushing rate. The flushing rate as a function of shear velocity u_* is estimated as $K_{sed}/\Delta z_{opd}$, where Δz_{opd} is the overall change in the oxygen penetration depth (~ 4 mm) with the tidal cycle (Figure 8). At the highest flow rate, the maximum flushing rate is 200 L m^{-2} d^{-1}, with the integrated average over the 44 h of eddy data is 72 L m^{-2} d^{-1}; this implies 14 days to flush 1 m of overlying water through the permeable sediment. These values agree with the flushing rate of 90 L m^{-2} d^{-1} estimated in coastal North Sea permeable sediments based on inert tracer experiments [*Janssen et al.*, 2005].

5.2. Hydrodynamic Forcing

The supply of O_2 to the investigated sediment is predominantly driven by the benthic hydrodynamics. This is evident by the relationship between the O_2 fluxes to the turbulence as $\varepsilon^{1/3}$ or u_* (Figure 9). Figure 9 shows the fit of the O_2 flux, F, with the LOW relationship

Figure 9. The EC oxygen flux as a function of the dissipation rate of TKE and u_*. For comparison, EC1 dissipations are scaled to 12 cm. EC1 data from 180 to 270° were omitted due to perceived frame interference (see Figure 4). The black line indicates the fit to the LOW equation (using a constant O_2 gradient), and the blue data are the modeled fluxes.

$$F = (\kappa z)^{4/3} \varepsilon^{1/3} \frac{\partial c}{\partial z} = \kappa u_* z \frac{\partial c}{\partial z}, \qquad (5)$$

for transport-limited sediment oxygen uptake [*Holtappels and Lorke*, 2011], where z is the measurement height (0.12 m) and the gradient $\frac{\partial c}{\partial z}$ seems to approach a relatively constant value ($\sim$0.3 μmol L^{-1} m^{-1}). Figure 9 also shows the model results, which follow the same trend. The model shows a slightly more varying O_2 gradient (increases by a factor of $\sim$2 over the full range as u_* increases). Both the model and the curve fit, however, suggest that changes in turbulent regimes through, e.g., higher flows or changes in bottom roughness (i.e., C_{1m} and z_o) are what predominately drives the transient increase in the O_2 flux to the sediment following the relationship shown in Figure 9.

Figure 6a demonstrates that the estimated bottom roughness C_{1m} (and z_o) varies substantially as a function of current speed due to various flow regimes and the presence of ripples. We show in equation (5) that the flux is proportional to u_*, which is dependent on C_{1m} as $u_* = C_{1m}^{1/2} u_{1m}$. C_{1m} doubles as the velocity magnitude increases from 3.5 to 10.2 cm s^{-1}. If we assume that this increase in C_{1m} is due to the ripples, then the ripples impart up to a $\sim$40% increase in u_*, and a subsequent 40% increase in benthic O_2 flux.

Furthermore, the parameterizations reported by *Berg et al.* [2007] for calculating the footprint contributing to the eddy flux signal, both the maximum footprint length, l, and the upstream distance of the strongest flux signal, x_{max}, are based on an assumption of a constant, flow-independent z_o. Our findings, however, suggest that the presence of ripples results in a flow-dependent z_o. The resulting footprint length therefore varies by a factor of over 3, and a factor of 5 in the distance to the flux maximum location—at least at our measuring conditions (Figure 6b). While the eddy assumptions state that the O_2 sink is homogeneous, changing flow speeds (and thus footprint sizes) could result in variable flux signals where the source is slightly heterogeneous.

5.3. Summary of Benthic Oxygen Fluxes
The combined-instrument average EC flux was -10.3 ± 6.3 mmol m^{-2} d^{-1} and generally agreed with what has been reported in the literature for sandy central North Sea sediments (Table 5). The standard deviation reported for the mean eddy flux is due to the large flux variability, which is dominated by boundary layer turbulence/flow velocity and sediment permeability. Both *Upton et al.* [1993] and *Lohse et al.* [1996] report similar values for their nearby study sites ($\sim$100 km SE of our location). Furthermore, *Lohse et al.* [1996] also report effective diffusivities of 5.3–18.7 times over molecular from their extracted cores, which is similar to the range we obtained (Figure 8). The deployed benthic chamber O_2 flux was -7.0 mmol m^{-2} d^{-1}, which was in the same range but slightly lower than the average EC flux from both instruments (-10.3 mmol m^{-2} d^{-1}). The chamber flux magnitude, however, is influenced by stirring rate in permeable sediments and could thus be conceivably closer to the EC fluxes with more energetic mixing [*Glud et al.*, 1996].

5.4. Modeling Pore Water and BBL O_2 Dynamics
To reproduce the magnitude and variability of the measured EC fluxes, we introduced enhanced bulk pore water diffusivity driven by the benthic hydrodynamics (equation (4)). Under this scenario, oxygen is essentially pumped into and "stored" in the sediment during the high flow (periods of high sediment diffusivity), which expands the sediment volume in which oxygen can be utilized. The supplied oxygen can then be consumed through the low-flow periods when much less (or no) O_2 is supplied deeper in the sediments. An example of this advective transport of oxygen deeper into permeable sediments was reported by *Cook et al.* [2007], who observed subsurface oxygen peaks as the water side advective supply ceases during low-flow periods, while intensified respiration exhausted the O_2 pool in the surface layers [see *Cook et al.*, 2007, Figure 9].

Table 5. Summary of Oxygen Fluxes (Flux), Standard Deviation (STD), % Difference Compared to Model Baseline (Diff), Local Sediment Oxygen Consumption Rate (R), and Water Depth

	Flux mmol m^{-2} d^{-1}	$\pm$STD mmol m^{-2} d^{-1}	Diff %	R mmol m^{-3} s^{-1}	Depth m
Measured EC1	−9.2	5.3			74
Measured EC2	−11.3	7.3			74
Model baseline	−11.4	6.7		0.05	74
Model 2 × R	−13.4	8.2	19	0.1	74
Model 0.5 × R	−9.4	5.6	−17	0.025	74
Model $D_s e^{0.5 \times \kappa u_*}$	−5.0	1.7	−57	0.05	74
Model $D_s e^{2 \times \kappa u_*}$	−49	44	334	0.05	74
Model 0.5 × O$_2$ at 1 m	−6.7	4.2	−41	0.05	
Model 1.5 × O$_2$ at 1 m	−15	9.0	35		
St7 [*Lohse et al.*, 1996]	−4.8			0.006	50
St7 [*Lohse et al.*, 1996]	−8.9			0.033	50
St4 [*Upton et al.*, 1993]	−10.3				81
St5 [*Upton et al.*, 1993]	−7.8				63

Using K$_{sed}$ from equation (4) in the model, together with a constant R (on the sediment side), consistently reproduced the EC flux magnitude and variability observed in our data (see Figure 7a) with excellent agreement ($r^2 > 0.94$). The below-described model sensitivity analysis is summarized in Table 5 and Figure 10. Using the model to mimic impermeable sediment by maintaining a constant pore water diffusivity (1× and 5 × D$_{sed}$) could not reproduce the observed variability (Figure 10).

The model was very sensitive to the effective pore water diffusivity; doubling α of the pore water diffusivity in equation (1) led to a 4.3-fold increase in the flux (−49 ± 44 mmol m^{-2} d^{-1}), while halving α led to just over a 50% reduction in flux (−5 ± 1.7 mmol m^{-2} d^{-1}; Table 5 and Figure 10). Changing the overlying O$_2$ concentration had a nearly proportional effect on the average fluxes, with a 50% decrease in O$_2$ resulting in a 41% decrease in flux (−6.7 ± 4.2 mmol m^{-2} d^{-1}) and a 50% increase leading to a 35% increase in flux (−15.2 ± 9 mmol m^{-2} d^{-1}).

Our selected sediment O$_2$ consumption rate (R) for the model was measured in the near coast, shallow region of the North Sea (Wadden Sea) [*Polerecky et al.*, 2005], and may not be representative for R in the central North Sea. Therefore we adjusted R by both 1/2 and 2 times the baseline value (Figure 7a) and found that modeled fluxes were not as sensitive to changes in R, with an average flux change of −17 and +19%, respectively. For model calibration, changes in the R value can thus be offset by a slight adjustment of the permeability in the opposite direction.

Our results suggest that even with a constant R, there is significant turbulence-driven flux variability within moderately permeable sediments. Interestingly, *Berg et al.* [2013] report only a 4 time increase in O$_2$ flux in permeable sediments measured with the EC for velocities from 0 to 20 cm s^{-1}, which they explain with a velocity-dependent R. Obviously, a constant R is a simplification; in reality, R will change over longer timescales as organic carbon is transported into the sediment and exhausted, or on shorter timescales as a result of a dynamic oxidation of reduced substances from deeper sediment layers [*Precht et al.*, 2004]. However, that does not affect the basic conclusion of a significant turbulence-driven oxic venting of the permeable surface sediments over the tidal cycles.
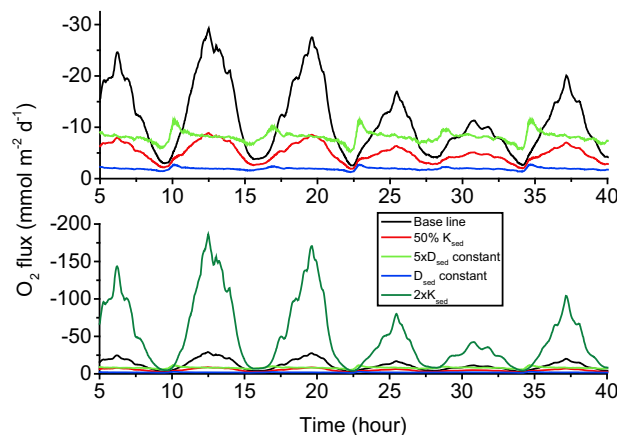

Figure 10. Modeling sensitivity analysis. The plots are the same except for the exclusion of the 2 × K$_{sed}$ curve (dark green) on the top figure for better scaling. The black line indicates the baseline flux shown in Figure 3c using the variable pore water diffusivity given by equation (1) (main text).

5.5. A Tidally Driven Perspective

Using the eddy correlation technique, combined with traditional benthic oxygen flux methods (chamber and microprofiles) and

modeling, yields new insights into the importance of bottom boundary layer turbulence for benthic O_2 availability and presumably the biogeochemical functioning of permeable coastal sediments. Using a suite of in situ approaches, it was possible to resolve nearly real-time in situ oxygen fluxes with a resolution and variability never observed before in permeable sediment. The obtained oxygen fluxes in the North Sea varied ∼25-fold over the tidal cycle due to what can be described as hydrodynamically driven pore water advection (represented here as enhanced bulk pore water diffusivity): oxygen is "stored" in the sediment during the high flow and expands the oxic sediment volume, which is then utilized during low-flow periods.

The calibrated benthic flux model forecasts that higher sustained bottom currents will result in deeper oxygen penetration depths and considerably higher fluxes. However, to maintain these higher fluxes, the increase in O_2 to the sediment would also have to accompany an increase of organic matter supply to the sediment pore water, among other factors. Nevertheless, our results suggest that hydrodynamic changes resulting in, e.g., altered current speeds could potentially impact bottom water seasonal oxygen levels. Changes in the physical oceanography of coastal systems have been suggested to increase their sensitivity to hypoxia [*Howarth et al.*, 2011]. Changing permeability could also affect the seasonal O_2 balance as sediment permeability can vary with time as the pores becomes clogged with bacteria and detritus (e.g., after spring bloom or pollutant runoff) until cleared through resuspension events (e.g., storms) [*Huettel et al.*, 2014].

According to modeling results (Figure 7b), regions within the sediment alternate between anoxic and oxic conditions on timescales ranging from minutes to hours over the daily tidal cycle, and even up to days over the spring-neap cycle. These oscillating redox conditions and variable oxygen penetration depth will have important implications for biogeochemical processes in the sediment. The redox dynamics would favor the growth of organisms having versatile metabolism, i.e., the ability to quickly shunt between different metabolic pathways. Redox oscillation can stimulate the degradation of complex (refractory) biogenic molecules [*Aller*, 1998] and associated pore water advection may enhance entrapment of labile organic material [*Huettel and Rusch*, 2000]. Furthermore, tidally driven advective pore water circulation and associated O_2 dynamics may affect ammonification, nitrification, and denitrification and thereby nutrient exchange and availability in permeable settings [*Gihring et al.*, 2010; *Kessler et al.*, 2012].

The present study underpins the importance of transient and dynamic oxygenation events in permeable sediments, and the turbulence and hydrodynamics that drives them, when evaluating the net effect for carbon and nutrient turnover. Therefore, combining various high-resolution physical and biogeochemical measurements in both the water column and at the sediment-water interface, coupled with our sediment-turbulence model, can provide further understanding of the biogeochemical and ecological functioning of these dynamic systems.

References

Aller, R. C. (1998), Mobile deltaic and continental shelf muds as suboxic, fluidized bed reactors, *Mar. Chem.*, *61*(3–4), 143–155.

Baldocchi, D. D. (2003), Assessing the eddy covariance technique for evaluating carbon dioxide exchange rates of ecosystems: Past, present and future, *Global Change Biol.*, *9*(4), 479–492.

Berg, P., N. Risgaard-Petersen, and S. Rysgaard (1998), Interpretation of measured concentration profiles in sediment pore water, *Limnol. Oceanogr.*, *43*(7), 1500–1510.

Berg, P., H. Roy, F. Janssen, V. Meyer, B. B. Jørgensen, M. Huettel, and D. de Beer (2003), Oxygen uptake by aquatic sediments measured with a novel non-invasive eddy-correlation technique, *Mar. Ecol. Prog. Ser.*, *261*, 75–83.

Berg, P., H. Roy, and P. L. Wiberg (2007), Eddy correlation flux measurements: The sediment surface area that contributes to the flux, *Limnol. Oceanogr. Methods*, *52*(4), 1672–1684.

Berg, P., M. H. Long, M. Huettel, J. E. Rheuban, K. J. McGlathery, R. W. Howarth, K. H. Foreman, A. E. Giblin, and R. Marino (2013), Eddy correlation measurements of oxygen fluxes in permeable sediments exposed to varying current flow and light, *Limnol. Oceanogr. Methods*, *58*(4), 1329–1343.

Bluteau, C. E., N. L. Jones, and G. N. Ivey (2011), Estimating turbulent kinetic energy dissipation using the inertial subrange method in environmental flows, *Limnol. Oceanogr. Methods*, *9*, 302–321.

Boudreau, B. P. (2000), The mathematics of early diagenesis: From worms to waves, *Rev. Geophys.*, *38*(3), 389–416.

Cheng, R. T., C. H. Ling, J. W. Gartner, and P. F. Wang (1999), Estimates of bottom roughness length and bottom shear stress in South San Francisco Bay, California, *J. Geophys. Res.*, *104*(C4), 7715–7728.

Cook, P. L. M., F. Wenzhöfer, R. N. Glud, F. Janssen, and M. Huettel (2007), Benthic solute exchange and carbon mineralization in two shallow subtidal sandy sediments: Effect of advective pore-water exchange, *Limnol. Oceanogr. Methods*, *52*(5), 1943–1963.

de Beer, D., F. Wenzhöfer, T. G. Ferdelman, S. E. Boehme, M. Huettel, J. E. E. van Beusekom, M. E. Böttcher, N. Musat, and N. Dubilier (2005), Transport and mineralization rates in North Sea sandy intertidal sediments, Sylt-Romo Basin, Wadden Sea, *Limnol. Oceanogr. Methods*, *50*(1), 113–127.

Emery, K. O. (1968), Relict sediments on continental shelves of the world, *Am. Assoc. Pet. Geol. Bull.*, *52*, 445–464.

Forster, S., M. Huettel, and W. Ziebis (1996), Impact of boundary layer flow velocity on oxygen utilisation in coastal sediments, *Mar. Ecol. Prog. Ser.*, *143*(1–3), 173–185.

Gihring, T. M., A. Canion, A. Riggs, M. Huettel, and J. E. Kostka (2010), Denitrification in shallow, sublittoral Gulf of Mexico permeable sediments, *Limnol. Oceanogr. Methods*, *55*(1), 43–54.

Glud, R. N. (2008), Oxygen dynamics of marine sediments, *Mar. Biol. Res.*, *4*(4), 243–289.

Glud, R. N., S. Forster, and M. Huettel (1996), Influence of radial pressure gradients on solute exchange in stirred benthic chambers, *Mar. Ecol. Prog. Ser.*, *141*(1–3), 303–311.

Glud, R. N., F. Wenzhöfer, A. Tengberg, M. Middelboe, K. Oguri, and H. Kitazato (2005), Distribution of oxygen in surface sediments from central Sagami Bay, Japan: In situ measurements by microelectrodes and planar optodes, *Deep Sea Res., Part I*, *52*(10), 1974–1987.

Glud, R. N., S. Rysgaard, G. Turner, D. F. McGinnis, and R. J. G. Leakey (2014), Biological- and physical-induced oxygen dynamics in melting sea ice of the Fram Strait, *Limnol. Oceanogr. Methods*, *59*(4), 1097–1111.

Goring, D. G., and V. I. Nikora (2002), Despiking acoustic Doppler velocimeter data, *J. Hydraul. Eng.*, *128*(1), 117–126.

Greenwood, N., et al. (2010), Detection of low bottom water oxygen concentrations in the North Sea: Implications for monitoring and assessment of ecosystem health, *Biogeosciences*, *7*(4), 1357–1373.

Gundersen, J. K., N. B. Ramsing, and R. N. Glud (1998), Predicting the signal of O_2 microsensors from physical dimensions, temperature, salinity, and O_2 concentration, *Limnol. Oceanogr.*, *43*(8), 1932–1937.

Holtappels, M., and A. Lorke (2011), Estimating turbulent diffusion in a benthic boundary layer, *Limnol. Oceanogr. Methods*, *9*, 29–41.

Holtappels, M., R. N. Glud, D. Donis, B. Liu, A. Hume, F. Wenzhöfer, and M. M. M. Kuypers (2013), Effects of transient bottom water currents and oxygen concentrations on benthic exchange rates as assessed by eddy correlation measurements, *J. Geophys. Res. Oceans*, *118*, 1157–1169, doi:10.1002/jgrc.20112.

Howarth, R., F. Chan, D. J. Conley, J. Garnier, S. C. Doney, R. Marino, and G. Billen (2011), Coupled biogeochemical cycles: Eutrophication and hypoxia in temperate estuaries and coastal marine ecosystems, *Front. Ecol. Environ.*, *9*(1), 18–26.

Huettel, M., and A. Rusch (2000), Transport and degradation of phytoplankton in permeable sediment, *Limnol. Oceanogr.*, *45*(3), 534–549.

Huettel, M., and I. T. Webster (2001), Porewater flow in permeable sediments, in *The Benthic Boundary Layer*, edited by B. P. Boudreau and B. B. Jørgensen, pp. 144–179, Oxford Univ. Press., N. Y.

Huettel, M., P. Berg, and J. E. Kostka (2014), Benthic exchange and biogeochemical cycling in permeable sediments, *Annu. Rev. Mar. Sci.*, *6*(8), 1–29.

Inoue, T., R. N. Glud, H. Stahl, and A. Hume (2011), Comparison of three different methods for assessing in situ friction velocity: A case study from Loch Etive, Scotland, *Limnol. Oceanogr. Methods*, *9*, 275–287.

Janssen, F., M. Huettel, and U. Witte (2005), Pore-water advection and solute fluxes in permeable marine sediments (II): Benthic respiration at three sandy sites with different permeabilities (German Bight, North Sea), *Limnol. Oceanogr. Methods*, *50*(3), 779–792.

Kessler, A. J., R. N. Glud, M. B. Cardenas, M. Larsen, M. F. Bourke, and P. L. M. Cook (2012), Quantifying denitrification in rippled permeable sands through combined flume experiments and modeling, *Limnol. Oceanogr. Methods*, *57*(4), 1217–1232.

Kundu, P. K., and I. M. Cohen (2008), *Fluid Mechanics*, 4th ed., Elsevier.

Lefebvre, A., V. B. Ernstsen, and C. Winter (2011), Influence of compound bedforms on hydraulic roughness in a tidal environment, *Ocean Dyn.*, *61*(12), 2201–2210.

Lohse, L., E. H. G. Epping, W. Helder, and W. van Raaphorst (1996), Oxygen pore water profiles in continental shelf sediments of the North Sea: Turbulent versus molecular diffusion, *Mar. Ecol. Prog. Ser.*, *145*(1–3), 63–75.

Lorke, A., and F. Peeters (2006), Toward a unified scaling relation for interfacial fluxes, *J. Phys. Oceanogr.*, *36*(5), 955–961.

Lorke, A., L. Umlauf, T. Jonas, and A. Wüest (2002), Dynamics of turbulence in low-speed oscillating bottom-boundary layers of stratified basins, *Environ. Fluid Mech.*, *2*(4), 291–313.

Lorke, A., D. F. McGinnis, A. Maeck, and H. Fischer (2012), Effect of ship locking on sediment oxygen uptake in impounded rivers, *Water Resour. Res.*, *48*, W12514, doi:10.1029/2012WR012483.

Lorke, A., D. F. McGinnis, and A. Maeck (2013), Eddy-correlation measurements of benthic fluxes under complex flow conditions: Effects of coordinate transformations and averaging time scales, *Limnol. Oceanogr. Methods*, *11*, 425–437.

Lorrai, C., D. F. McGinnis, P. Berg, A. Brand, and A. Wüest (2010), Application of oxygen eddy correlation in aquatic systems, *J. Atmos. Ocean. Technol.*, *27*(9), 1533–1546.

McCann-Grosvenor, K., C. E. Reimers, and R. D. Sanders (2014), Dynamics of the benthic boundary layer and seafloor contributions to oxygen depletion on the Oregon inner shelf, *Cont. Shelf Res.*, *84*, 93–106.

McGinnis, D. F., P. Berg, A. Brand, C. Lorrai, T. J. Edmonds, and A. Wüest (2008), Measurements of eddy correlation oxygen fluxes in shallow freshwaters: Towards routine applications and analysis, *Geophys. Res. Lett.*, *35*, L04403, doi:10.1029/2007GL032747.

McGinnis, D. F., S. Cherednichenko, S. Sommer, P. Berg, L. Rovelli, R. Schwarz, R. N. Glud, and P. Linke (2011), Simple, robust eddy correlation amplifier for aquatic dissolved oxygen and hydrogen sulfide flux measurements, *Limnol. Oceanogr. Methods*, *9*, 340–347.

Moncrieff, J., R. Clement, J. Finnigan, and T. Meyers (2004), Averaging, detrending, and filtering of eddy covariance time series, in *Handbook of Micrometeorology: A Guide for Surface Flux Measurement and Analysis*, edited by X. Lee, W. J. Massman, and B. E. Law, Kluwer Acad., Dordrecht, Netherlands.

Pfannkuche, O., and P. Linke (2003), GEOMAR Landers as long-term deep-sea observatories, *Sea Technol.*, *44*(9), 50–55.

Polerecky, L., U. Franke, U. Werner, B. Grunwald, and D. de Beer (2005), High spatial resolution measurement of oxygen consumption rates in permeable sediments, *Limnol. Oceanogr. Methods*, *3*, 75–85.

Precht, E., and M. Huettel (2003), Advective pore-water exchange driven by surface gravity waves and its ecological implications, *Limnol. Oceanogr. Methods*, *48*(4), 1674–1684.

Precht, E., U. Franke, L. Polerecky, and M. Huettel (2004), Oxygen dynamics in permeable sediments with wave-driven pore water exchange, *Limnol. Oceanogr. Methods*, *49*(3), 693–705.

Reimers, C. E., H. A. Stecher, G. L. Taghon, C. M. Fuller, M. Huettel, A. Rusch, N. Ryckelynck, and C. Wild (2004), In situ measurements of advective solute transport in permeable shelf sands, *Cont. Shelf Res.*, *24*(2), 183–201.

Reimers, C. E., H. T. Ozkan-Haller, P. Berg, A. Devol, K. McCann-Grosvenor, and R. D. Sanders (2012), Benthic oxygen consumption rates during hypoxic conditions on the Oregon continental shelf: Evaluation of the eddy correlation method, *J. Geophys. Res.*, *117*, C02021, doi: 10.1029/2011JC007564.

Revsbech, N. P. (1989), An oxygen microsensor with a guard cathode, *Limnol. Oceanogr.*, *34*(2), 474–478.

Rocha, C. (2008), Sandy sediments as active biogeochemical reactors: Compound cycling in the fast lane, *Aquat. Microb. Ecol.*, *53*(1), 119–127.

Rusch, A., S. Forster, and M. Huettel (2001), Bacteria, diatoms and detritus in an intertidal sandflat subject to advective transport across the water-sediment interface, *Biogeochemistry*, *55*(1), 1–27.

Santos, I. R., B. D. Eyre, and M. Huettel (2012), The driving forces of porewater and groundwater flow in permeable coastal sediments: A review, *Estuarine Coastal Shelf Sci.*, *98*, 1–15.

Scalo, C., U. Piomelli, and L. Boegman (2012), Large-eddy simulation of oxygen transfer to organic sediment beds, *J. Geophys. Res.*, *117*, C06005, doi:10.1029/2011JC007289.

Scalo, C., L. Boegman, and U. Piomelli (2013), Large-eddy simulation and low-order modeling of sediment-oxygen uptake in a transitional oscillatory flow, *J. Geophys. Res. Oceans*, *118*, 1926–1939, doi:10.1002/jgrc.20113.

Schmale, O., M. Haeckel, and D. F. McGinnis (2011), Response of the Black Sea methane budget to massive short-term submarine inputs of methane, *Biogeosciences*, *8*(4), 911–918.

Schneider von Deimling, J. S., G. Rehder, J. Greinert, D. F. McGinnis, A. Boetius, and P. Linke (2011), Quantification of seep-related methane gas emissions at Tommeliten, North Sea, *Cont. Shelf Res.*, *31*(7–8), 867–878.

Ullman, W. J., and R. C. Aller (1982), Diffusion-coefficients in nearshore marine-sediments, *Limnol. Oceanogr.*, *27*(3), 552–556.

Upton, A. C., D. B. Nedwell, R. J. Parkes, and S. M. Harvey (1993), Seasonal benthic microbial activity in the southern north-sea; oxygen-uptake and sulfate reduction, *Mar. Ecol. Prog. Ser.*, *101*(3), 273–281.

Werner, U., M. Billerbeck, L. Polerecky, U. Franke, M. Huettel, J. E. E. van Beusekom, and D. de Beer (2006), Spatial and temporal patterns of mineralization rates and oxygen distribution in a permeable intertidal sand flat (Sylt, Germany), *Limnol. Oceanogr. Methods*, *51*(6), 2549–2563.

Weston, K., L. Fernand, J. Nicholls, A. Marca-Bell, D. Mills, D. Sivyer, and M. Trimmer (2008), Sedimentary and water column processes in the Oyster Grounds: A potentially hypoxic region of the North Sea, *Mar. Environ. Res.*, *65*(3), 235–249.

Wilczak, J. M., S. P. Oncley, and S. A. Stage (2001), Sonic anemometer tilt correction algorithms, *Boundary Layer Meteorol.*, *99*(1), 127–150.

Wüest, A., and A. Lorke (2003), Small-scale hydrodynamics in lakes, *Annu. Rev. Fluid Mech.*, *35*, 373–412.